INFLUENCE OF LOAD INTRODUCTION METHOD ON WINGBOX OPTIMIZATION WITH NONLINEAR STRUCTURAL STABILITY CONSTRAINTS

Francesco M. A. Mitrotta[1], Alberto Pirrera[1], Terence Macquart[1], Jonathan E. Cooper[1],
Alex Pereira do Prado[2], Pedro Higino Cabral[2]

[1]University of Bristol
Queen's Building, University Walk, Bristol BS8 1TR, UK
fma.mitrotta@bristol.ac.uk
alberto.pirrera@bristol.ac.uk
terence.macquart@bristol.ac.uk
j.e.cooper@bristol.ac.uk

[2]Embraer S.A.
São José dos Campos, São Paulo, 12227-901, Brazil
alex.prado@embraer.com.br
pedro.cabral@embraer.com.br

Keywords: Aeroelastic optimization, nonlinear structural stability, wingbox structures.

Abstract: The aviation industry's challenge to achieve net-zero carbon emissions by 2050 demands innovative approaches to aircraft design, particularly through the development of lighter, more fuel-efficient aircraft structures. Aeroelastic optimization plays a crucial role in this process by enabling exploration within a design space bounded by numerous constraints, including structural strength and stability. Traditional aeroelastic optimizations rely on linear buckling analyses which, while computationally efficient, tend to over-constrain the design space due to their conservative nature. Such conservatism places a glass ceiling on the sizing loads used within optimization studies, preventing the exploitation of the full load-bearing capacity, especially as aircraft designs trend towards more slender and compliant wing structures where nonlinear effects become significant. This paper builds on previous research by integrating a nonlinear structural stability constraint into the optimization of a wingbox structure under a distributed load. Three optimization scenarios are considered to evaluate the influence of different load introduction methods: distributed non-follower forces, distributed follower forces, and non-follower forces applied to a load reference axis. In addition, the formulation of the nonlinear structural stability constraint is revisited to allow its application in presence of follower forces. Our findings, demonstrated on an idealized version of the Common Research Model wingbox, confirm a substantial mass reduction using the nonlinear constraints compared to the traditional linear ones, ranging between 8 and 9%. Not much difference is found between the structures optimized with distributed non-follower and follower forces, because of their small deflections. Instead, a noticeable difference is found for the structure optimized with non-follower forces applied to the load reference axis, which achieves a smaller mass reduction. If on one hand these results suggest that employing the load reference axis approach might lead to conservative results, on the other hand we show that such approach leads to an inaccurate prediction of the structural deformation.

1 INTRODUCTION

In 2021, the Air Transport Action Group established an ambitious target for global civil aviation to reach net-zero carbon emissions by 2050 [1], aligning with the Paris Agreement's aim to keep global warming below 1.5 °C. This objective presents a significant challenge for the aviation industry, necessitating innovative approaches to aircraft design.

The objective of net-zero aviation has given new impetus to the development of fuel-efficient aircraft. As conceptually outlined by the Breguet Range equation, emission reductions can be achieved through lighter aircraft, improved aerodynamics, and increased engine efficiency [2]. Recent decades have seen significant advancements in aeroelastic optimization tools for the design of lightweight structures, primarily driven by the development and integration of composite materials, which are known for their high specific strength and stiffness and extensive elastic tailoring capabilities.

In aeroelastic optimizations, static structural stability often emerges as a pivotal constraint [3–15]. Typically, linear buckling analyses are employed to impose this constraint, which involve eigenvalue problems based on the linearization of the structural response around the undeformed configuration. These analyses, while computationally efficient and simple to implement, tend to over-constrain the design space, potentially leading to over-designed structures. In fact, in advanced design stages, aerospace structures are sized to bear loads beyond their linear buckling point [16].

In a recent work [17], we proposed the hypothesis that, in current aeroelastic optimizations, linear buckling evaluations place a glass ceiling on the sizing load that the wing structure can carry, curtailing in this way the maximum load-carrying capacity. This limitation is particularly relevant in the context of evolving wing designs driven by the pursuit of sustainability, where the increasing slender and compliant nature of wings makes nonlinear effects more significant. Accordingly, we argue that nonlinear evaluations of structural stability could lead to more efficient design solutions.

In the same study, we demonstrated a novel nonlinear structural stability constraint for the optimization of wingbox structures [17]. The approach was based on enforcing the positive-definiteness of the tangent stiffness matrix by monitoring its smallest magnitude eigenvalues for all the increments of the nonlinear analysis and by imposing their positivity.

This concept was proven through a structural optimization of an idealized model of the Common Research Model (CRM) [18] wingbox, hereinafter referred to as the CRM-like box beam, employing a concentrated tip load and a uniform wall thickness. The optimization with nonlinear structural stability constraints achieved an 11.3% mass reduction compared to a baseline structure optimal in linear buckling terms. In a more recent work [19], we increased the realism of the optimization scenario using a linearly varying thickness over the length of the same model, showing a 29.6% mass reduction with respect to the linearly optimized structure.

As a further step towards fully-coupled aeroelastic optimization on a realistic wing model, this paper builds on our previous works applying the nonlinear structural stability constraint to a problem with distributed load over the top and bottom skin of the CRM-like box beam, with the idea of loosely mimicking an aerodynamic load. However, real aerodynamic loads are generated by the pressure exerted by the flow field, meaning that they

are in effect follower loads. This poses a challenge from a nonlinear structural stability perspective, as follower loads are non-conservative, implying a non-symmetric tangent stiffness matrix and a broken relationship with the total potential energy. Consequently, it is no longer possible to assess structural stability by looking at the eigenvalues of the non-symmetric tangent stiffness matrix.

At the same time, many aeroelastic frameworks employ simplified methods such as Vortex Lattice Method (VLM) or Doublet Lattice Method (DLM) to calculate the aerodynamic loads. These methods approximate the wing by representing it as a mean aerodynamic surface and compute the net lifting pressure over this surface. The introduction of the aerodynamic loads into the structure is typically achieved by condensing the load on a load reference axis (LRA). When the structure is represented by a beam model the LRA is coincident with the structural model itself [20], while in case of a shell model the LRA is constructed artificially, for example adding fictitious nodes at the center of the rib sections [3]. However, the validity of this type of approach for the assessment of nonlinear structural stability is an open question.

In this paper we address the above-mentioned challenges and questions by redefining the nonlinear structural stability constraint to include cases with follower loads and by investigating the influence of different load introduction methods on the optimization of the CRM-like box beam under nonlinear structural stability constraints. We consider three different load introduction methods: distributed non-follower forces, distributed follower forces, and non-follower forces applied to the LRA. For each method we perform a first optimization with linear buckling constraints and a second optimization with nonlinear structural stability constraints, starting from the linearly optimized structure.

The remainder of the paper is structured as follows: Sec. 2 provides the theoretical background on the nonlinear structural stability constraint, including the case of follower loads. Section 3 presents the numerical model and the definition of the optimization problems. Finally, Sec. 4 addresses the investigation on the influence of the load introduction method on both the initial structure and on the optimization results.

The results herein can be reproduced through an open-source Jupyter notebook available in a GitHub repository[1], where additional resources on this research are also available.

2 NONLINEAR STRUCTURAL STABILITY CONSTRAINT

2.1 Conservative loads

To calculate equilibrium points and assess their stability in the geometrically nonlinear analysis of structures under conservative loads, it is necessary to consider the total potential energy, Π, which is given by the difference between the internal strain energy, U, and the external work done [21], W, i.e.

$$\Pi = U - W. \tag{1}$$

In general, the total potential energy is a function of the state parameters, $\boldsymbol{u}$, corresponding to the structural degrees of freedom, and other parameters such as the applied loads, $\boldsymbol{p}$, whence $\Pi = \Pi\left(\boldsymbol{u}, \boldsymbol{p}\right)$.

---

[1]https://github.com/fmamitrotta/nonlinear-structural-stability-notebooks, accessed April 2024.

Equilibrium is found at points where the potential energy has a stationary value, or in other words where its first derivative with respect to the states is zero, such that

$$\frac{\partial \Pi}{\partial \boldsymbol{u}} = \boldsymbol{0}. \tag{2}$$

The stability of the equilibrium points depends on the second derivative of the potential energy with respect to the state parameters. This means that we need to consider the Hessian of the potential energy, which corresponds to the tangent stiffness matrix, so

$$\frac{\partial^2 \Pi}{\partial \boldsymbol{u}^2} = \boldsymbol{H}_\Pi = \boldsymbol{K}_T. \tag{3}$$

The tangent stiffness matrix represents the local, point-wise tangent to the load-displacement manifold and changes at every equilibrium point found during the nonlinear analysis. The stability of an equilibrium point is thus established as

$$\boldsymbol{K}_T\left(\boldsymbol{u}\right) \begin{cases} \text{positive definite} \Rightarrow \text{stable equilibrium;} \\ \text{singular} \Rightarrow \text{neutral equilibrium;} \\ \text{indefinite or negative definite} \Rightarrow \text{unstable equilibrium.} \end{cases} \tag{4}$$

In the context of an aircraft wing, it is desirable that the structure is always loaded along a stable equilibrium path. Traversing unstable equilibria may indeed cause sudden snap-throughs, which, be it local or global, may cause structural damage. For this reason, the nonlinear structural stability constraint employed here consists in constraining the tangent stiffness matrix to be positive definite for all converged increments of the nonlinear analysis, or in other words, for all the calculated equilibrium points.

The definiteness of a matrix can be evaluated by considering its eigenvalues. Consequently, we can recast Eq. (4) as

$$\boldsymbol{K}_T\left(\boldsymbol{u}\right) \begin{cases} \text{all eigenvalues} > 0 \Rightarrow \text{stable equilibrium;} \\ \text{at least one eigenvalue} = 0 \Rightarrow \text{neutral equilibrium;} \\ \text{at least one eigenvalue} < 0 \Rightarrow \text{unstable equilibrium}^2. \end{cases} \tag{5}$$

Equation (5) means that we can evaluate the nonlinear structural stability of the structure by monitoring the eigenvalues, λ, of the tangent stiffness matrix for each converged increment of the nonlinear analysis. However, the size of the tangent stiffness matrix of typical Finite Element (FE) models employed in aeroelastic optimizations makes the computation of all eigenvalues impractical. For this reason, only the N_λ smallest magnitude eigenvalues are monitored, and they are constrained to remain positive.

---

[2]In the case of at least one zero and one negative eigenvalue occurring simultaneously, the equilibrium is neutral along the principal stiffness directions associated with the zero eigenvalues and unstable along the principal stiffness directions associated with the negative eigenvalues. Consequently, the structure is considered unstable overall.

2.2 Non-conservative loads

For non-conservative loads, such as those induced by aerodynamic forces in flight, the external work done on the structure cannot be described by a potential energy function, since it is no longer path-independent. This deviation from conservative principles leads to two major ramifications: the tangent stiffness matrix $\boldsymbol{K}_T$ is non-symmetric, and a total potential energy of the system does not exist, meaning that there is no direct relationship between stability and tangent stiffness matrix. Consequently, Eq.(5) cannot be applied to infer stability and enforce the nonlinear structural stability constraint.

The mixed perturbation stability criterion [22] offers a solution to this issue by allowing stability analysis through the symmetric part of the tangent stiffness matrix, denoted as $\boldsymbol{K}_{T_s}$ and obtained as

$$\boldsymbol{K}_{T_s} = \frac{\boldsymbol{K}_T + \boldsymbol{K}_T^\intercal}{2}. \tag{6}$$

This criterion defines the structural system to be statically stable if the linear system

$$\delta\boldsymbol{p} = \boldsymbol{K}_T\delta\boldsymbol{x} \tag{7}$$

is non-singular for all mixed perturbation $(\delta p_1, \ldots, \delta p_k, \delta x_{k+1}, \ldots, \delta x_n)$, where δp_i are the infinitesimal perturbations of the loads and δx_i are the incremental displacements resulting from the new equilibrium of the system.

For Eq. (7) to be non-singular for all mixed perturbation, the expression

$$\delta\boldsymbol{x}^\intercal\delta\boldsymbol{p} > 0 \tag{8}$$

must hold. By substituting Eq. (7) into Eq. (8), we obtain the quadratic form

$$\delta\boldsymbol{x}^\intercal\boldsymbol{K}_T\delta\boldsymbol{x} > 0. \tag{9}$$

The above condition means that if the quadratic form of the tangent stiffness matrix at a given equilibrium point is positive definite, then the equilibrium is stable.

The positive definiteness of the quadratic form $\delta\boldsymbol{x}^\intercal\boldsymbol{K}_T\delta\boldsymbol{x}$ can be assessed by looking at the quadratic form of the symmetric part of the tangent stiffness matrix, as for all $\delta\boldsymbol{x} \in \mathbb{R}$

$$\delta\boldsymbol{x}^\intercal\boldsymbol{K}_T\delta\boldsymbol{x} = \delta\boldsymbol{x}^\intercal\boldsymbol{K}_{T_s}\delta\boldsymbol{x}. \tag{10}$$

In practical terms, this means that for the case of non-conservative loads, Eq. (5) becomes

$$\boldsymbol{K}_{T_s}(\boldsymbol{u}) \begin{cases} \text{all eigenvalues} > 0 \Rightarrow \text{stable equilibrium;} \\ \text{at least one eigenvalue} = 0 \Rightarrow \text{neutral equilibrium;} \\ \text{at least one eigenvalue} < 0 \Rightarrow \text{unstable equilibrium.} \end{cases} \quad (11)$$

In other words, to enforce the nonlinear structural stability constraint in presence of non-conservative loads, we must symmetrize the tangent stiffness matrix at every equilibrium point, calculate the N_λ smallest magnitude eigenvalues and constrain these to remain positive.

2.3 Nonlinear solver

The way in which a structure's equilibrium manifold is traced depends on the method employed to solve the nonlinear governing equilibrium equation. Herein, we focus on static analyses and we require the nonlinear solver to be able to follow both stable and unstable paths to provide a robust approach for the evaluation of the nonlinear stability constraint function.

In the more general case of non-conservative loads, the nonlinear equilibrium equations of a structure can be expressed as a force balance between internal and external forces

$$\boldsymbol{R}(\boldsymbol{u}, \mu) = \boldsymbol{f}(\boldsymbol{u}) - \boldsymbol{p}(\boldsymbol{u}, \mu) = \boldsymbol{f}(\boldsymbol{u}) - \mu \hat{\boldsymbol{p}}(\boldsymbol{u}) = \boldsymbol{0} \quad (12)$$

where $\boldsymbol{R}$ is a residual, $\boldsymbol{u}$ is the displacement vector, μ a scalar loading parameter, $\boldsymbol{f}$ the vector of internal forces, which is only dependent on $\boldsymbol{u}$, and $\boldsymbol{p}$ the vector of non-conservative external forces, depending both on μ and $\boldsymbol{u}$. The external forces can be expressed in terms of a force vector $\hat{\boldsymbol{p}}$, purely dependent on the displacements, multiplied by the loading parameter μ, independent of the displacements, as in nonlinear problems the external loads are usually applied in increments. In the case of purely conservative loads, the force vectors $\boldsymbol{p}$ and $\hat{\boldsymbol{p}}$ are independent of the displacements.

The aeroelastic optimization frameworks that feature nonlinear structural analysis, typically employ load control methods to solve Eq. (12) [12, 15]. With this approach, a load value is imposed at every consecutive increment of the nonlinear analysis and held constant during Newton-Raphson iterations until convergence is achieved. Upon convergence, the analysis moves on to the next load increment. This method has issues with load limit point bifurcations, because it cannot follow the unstable segment of the equilibrium path beyond the limit point, where the applied load decreases. In fact, the solver might jump to the next available equilibrium point for the new increment above the limit point, or it might not achieve convergence at all [23]. In both cases load controlled increments cannot find unstable equilibrium points, making them unsuitable for an aeroelastic optimization framework that aims to evaluate structural stability with nonlinear methods. Similar problems are faced by displacement-controlled solutions, but at displacement limit points.

Considering the above requirements, the chosen strategy for the solution of Eq. (12) is path-following with arc-length control. In this approach, the solution path is traced with an incremental-iterative method that imposes a simultaneous variation of load and displacement variables for the solution of the linearized equilibrium equations. The ith

equilibrium point is searched at an arc-length distance Δs^i from the last known equilibrium, Δs^i being calculated via a norm of the increment $(\Delta \mathbf{u}^i, \Delta \mu^i)$. The iterations are constrained to lie on the surface created by the arc, and they eventually converge at the intersection of the arc and the equilibrium path. In this way, arc-length methods can successfully calculate the equilibrium path of a structure also in presence of instabilities like limit point bifurcations [23]. Consequently, the arc-length method is chosen for the evaluation of the nonlinear structural stability constraint employed in this paper, as it can successfully follow stable as well unstable segments of an equilibrium path.

When linearizing Eq. (12) to find a solution at the j-th iteration of the i-th increment, the tangent stiffness matrix appears in the form of

$$\boldsymbol{K}_{T,j-1}^i \delta \boldsymbol{u}_j^i = \delta \mu_j^i \hat{\boldsymbol{p}} - \boldsymbol{R}_{j-1}^i, \tag{13}$$

where $\delta \boldsymbol{u}_j^i$ and $\delta \mu_j^i$ respectively represent the differential displacements and scalar loading parameter between the current iteration, j, and the last iteration, $j-1$.

Equation (13) is coupled with the equation that constrains the iterations to lie on the surface created by the above-mentioned arc to find $\delta \boldsymbol{u}_j^i$ and $\delta \mu_j^i$, requiring the inversion or the factorization of $\boldsymbol{K}_{T,j-1}^i$. In presence of non-conservative loads, this matrix is non-symmetric, which makes this operation more computationally expensive. However, it is not strictly necessary to use the non-symmetric stiffness matrix during the iterations to achieve convergence [24]. Since we need to symmetrize the tangent stiffness matrix at every equilibrium point to assess the structural stability, in the analyses of Sec. 4 we use the symmetrized matrix also during the incremental-iterative procedure of the arc-length method with the aim of easing the computational burden.

3 DEFINITION OF THE STRUCTURAL MODEL AND OF THE OPTIMIZATION PROBLEMS

In this section, we define the numerical model of the CRM-like box beam, the different load introduction methods used for the optimizations discussed in Sec. 4 and the optimization problems with linear buckling and nonlinear structural stability constraints.

3.1 The CRM-like box beam model

The CRM-like box beam is a straight box beam idealization of the CRM wingbox based on the data provided in [25]. It was developed for a previous study [17], where its sizing is reported, to obtain a relatively simple representation of a typical wingbox structure used in aeroelastic optimizations. To investigate the nonlinear structural stability response, the model was developed to retain only the essential features that influence such response, that is to say ribs and skin stiffeners. Specifically, the CRM-like box beam is reinforced by 19 equally spaced ribs and 2 equally spaced stiffeners on each skin. The model's geometry and dimensions are depicted in Fig. 1, while the cross-sectional and material properties of the model are summarized in Table 1.

The numerical model is implemented in MSC Nastran, where all geometrical parts are discretized using CQUAD4 (thin shell) elements. Fixed boundary conditions are enforced at the root section by means of a SPC1 card.
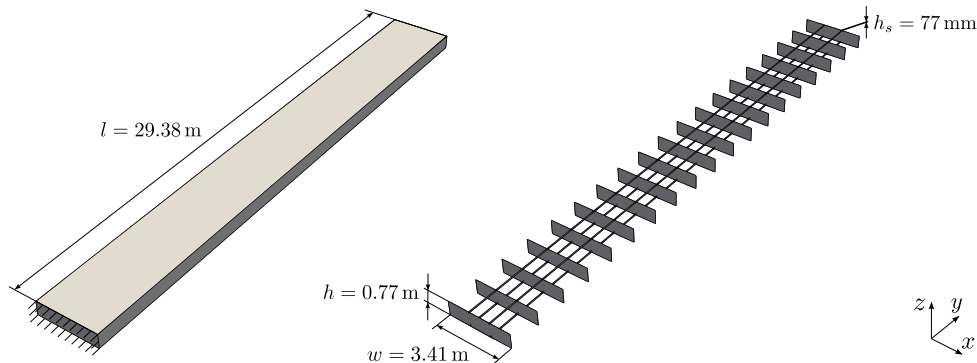
Figure 1: Geometry and dimensions of the CRM-like box beam model.

Table 1: CRM-like box beam cross-sectional and material properties. Material properties from [26]. The same thickness is used for all structural parts: skin, spars, ribs and stiffeners.

Parameter	Value
Wall thickness	7.7 mm
Density	2780 kg/m^3
Young's modulus	$73.1 \cdot 10^9$ Pa
Poisson's ratio	0.3
Yield strength	$420 \cdot 10^6$ Pa

3.2 Load introduction methods

To study the influence of different load introduction methods on the nonlinear structural stability analysis and optimization of the CRM-like box beam, we consider three different cases: distributed non-follower forces, distributed follower forces, and non-follower forces applied to a LRA. In the first two cases, we use an elliptical load distribution over both the top and bottom skin of the CRM-like box beam, with the aim of loosely mimicking the aerodynamic load applied to a wing. In the last case, we use the Matching-based Extrapolation of Loads and Displacements (MELD) transfer scheme [27][3] to define the load on the LRA.

For the application of distributed non-follower forces, the load is introduced in the Nastran model using FORCE cards at every node on the top and bottom skin, which define non-follower nodal forces. Figure 2(a) illustrates this load introduction approach.

In the case of distributed follower forces, the load is introduced via PLOAD2 cards defined on every quadrilateral element of the top and bottom skin. Each PLOAD2 card specifies a pressure load, which is transformed by Nastran into four equal follower-forces at the nodes of the element. This method results in a load distribution very similar to that of the non-follower forces, with minor deviations at the skin edges.

For the application of non-follower forces to the LRA, we construct a virtual axis by placing new nodes at the center of each rib and by connecting each of these nodes to the nodes at the edges of the corresponding rib using RBE3 elements. These elements create multipoint constraints that distribute the load from the central node to the connected nodes and calculate the displacement of the former as a weighted average of the displace-

---

[3]MELD is available as part of the FUNtoFEM coupling framework, publicly accessible at https://github.com/smdogroup/funtofem (accessed May 2024).

8

ments of the latter. The MELD scheme is used to transfer the distributed non-follower forces on the skin to the nodes of the LRA in a way that enforces energy conservation.

Typically, MELD defines the load and displacement transfer between an aerodynamic and a structural mesh by linking each aerodynamic surface node to a set of nearest structural nodes and determining an optimal rigid rotation and translation through a weighted least-squares problem. In our case, we use the mesh of the CRM-like box beam as a pseudo-aerodynamic mesh, and the nodes of the LRA as a pseudo-structural mesh. To provide MELD with the pseudo-structural displacements needed to set up the load transfer scheme, we perform a linear analysis using the distributed non-follower forces, and we find the displacements of the nodes on the LRA. Successively, we transfer the load from the mesh of the CRM-like box beam to the nodes of the LRA and we apply it using FORCE cards, as shown in Fig. 2(b).
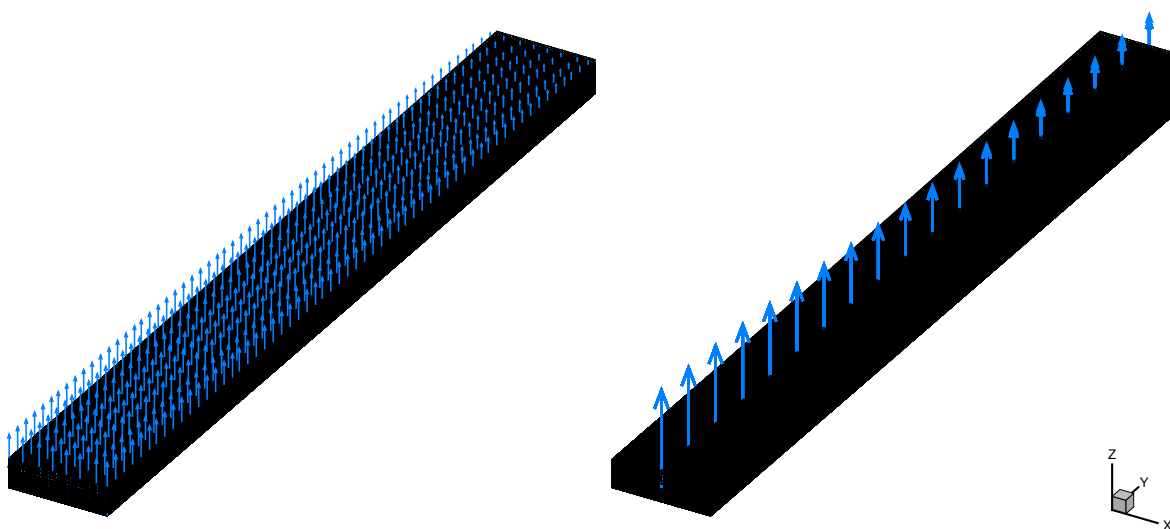
(a) Distributed non-follower forces. Vectors are sub-sampled for the sake of clarity.

(b) Non-follower forces applied to LRA.

Figure 2: Static load applied to CRM-like box beam.

A mesh convergence study was conducted on the model loaded with distributed non-follower forces to determine an appropriate mesh size that balances computational efficiency with accuracy. The final converged mesh consists of approximately $3.3 \cdot 10^4$ elements and results in a linear buckling load of about $3.0 \cdot 10^4$ N. The critical buckling mode for this configuration is depicted in Fig. 3, which also highlights the node experiencing the largest displacement. The displacement along the z-axis at this node is used to monitor the local out-of-plane displacements over the root region in the nonlinear analyses.

Further details on the mesh convergence study are reported in the Appendix.

3.3 Optimization problems

For each load introduction method we perform two subsequent mass-minimization optimizations: one with linear buckling constraints and the other with nonlinear structural stability constraints. We use the same design load for all optimizations, choosing it to be equal to the linear buckling load obtained for the initial structure under distributed non-follower forces.

Analogously to our last work [19], we allow only the wall thickness to change during the optimization, imposing a linear variation along length of the CRM-like box beam, which is defined by two design variables: the thickness at the root, t_{root}, and the thickness at the tip, t_{tip}. As shown in Fig. 4, the structure is divided into design segments with uniform thickness, corresponding to either ribs or box beam sections including spars, skin and stiffeners. The thickness of each segment is obtained by means of a linear interpolation between t_{root} and t_{tip} and by evaluating the thickness value at the center of each design segment.

The first optimization of the CRM-like box beam employs linear buckling constraints and serves to define a baseline structure for the optimization with nonlinear structural stability constraints. The objective is to minimize the mass of the initial CRM-like box beam while ensuring that the linear buckling load is larger than the design load and that the deformations remain elastic. All computations are performed using MSC Nastran's linear buckling solution sequence, SOL 105. The first constraint is implemented by computing the 20 smallest positive buckling load factors, representing the ratio between the buckling load and the applied load, $BLF = P_{\text{SOL 105}}/P_{\text{design}}$, and by imposing that they are all larger than 1. The second constraint is implemented by enforcing that the von Mises
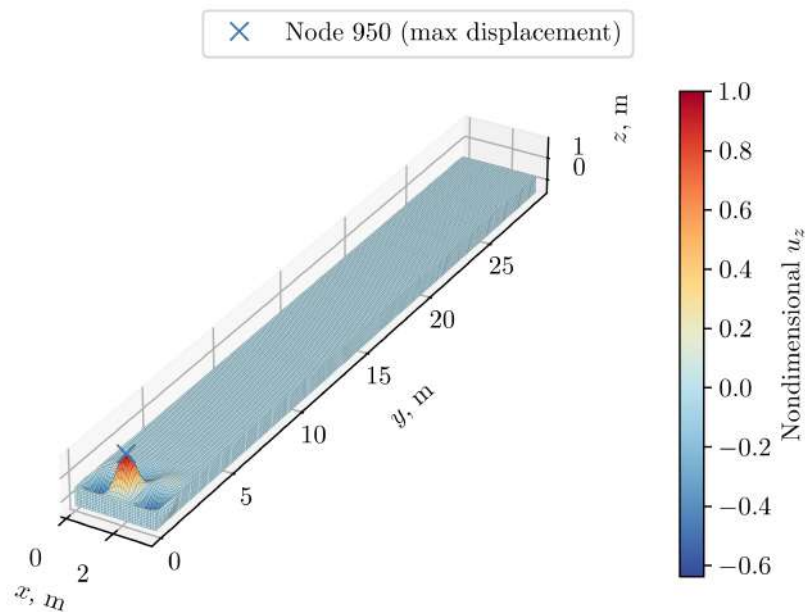
Figure 3: Critical buckling mode of the initial structure under distributed non-follower forces.
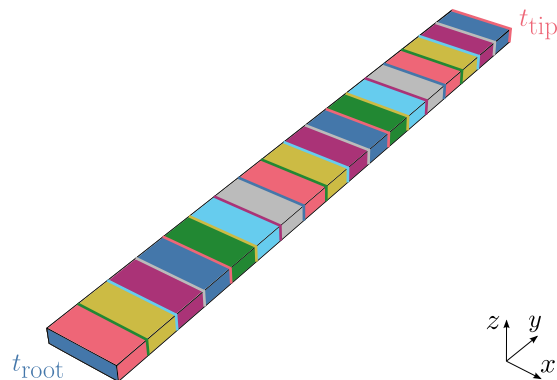
Figure 4: Design segments.

10

stress of each element is smaller than the yield strength of the material.

In summary, the optimization problem with linear buckling constraints is defined as

$$
\begin{aligned}
\text{minimize} \quad & m \\
\text{by varying} \quad & t_{\min} \leq [t_{\text{root}},\, t_{\text{tip}}] \leq t_{\max} \\
\text{subject to} \quad & g_{BLF,i} = 1 - BLF_i < 0 \quad i = 1, \ldots, N_{BLF} \\
& g_{\sigma,j} = \sigma_j - \sigma_{\max} < 0 \qquad j = 1, \ldots, N_e
\end{aligned}
\tag{14}
$$

where $t_{\min}$ and $t_{\max}$ are the thickness bounds, which are set between 1 and $20\,\text{mm}$, BLF_i is the i-th buckling load factor, with $N_{BLF} = 20$, σ_j is the von Mises stress of the j-th element, evaluated at both the top and bottom plane of the element, and $\sigma_{\max}$ is the yield strength of the material.

Instead of imposing the constraints separately on each buckling load factor and on each element, they are aggregated using Kreisselmeier–Steinhauser (KS) functions [28], such that

$$
KS_{BLF} = \max_i \left(g_{BLF,i} \right) + \frac{1}{\rho} \ln \left(\sum_{i=1}^{N_{BLF}} \exp \left(\rho \left(g_{BLF,i} - \max_i \left(g_{BLF,i} \right) \right) \right) \right)
\tag{15}
$$

$$
KS_\sigma = \max_j \left(g_{\sigma,j} \right) + \frac{1}{\rho} \ln \left(\sum_{j=1}^{N_e} \exp \left(\rho \left(g_{\sigma,j} - \max_k \left(g_{\sigma,j} \right) \right) \right) \right)
\tag{16}
$$

where ρ is the aggregation factor determining how close the KS function is to the maximum function, which is set to 100. This aggregation technique returns a single value for each constraint, representing an envelope of all the calculated quantities.

The structure obtained from the optimization with linear buckling constraints is used as starting point for the optimization with the nonlinear structural stability constraint. The latter is implemented by imposing that the 20 smallest magnitude eigenvalues of the tangent stiffness matrix, or of its symmetric part, are positive for all converged increments along the traced equilibrium path. The constraint on von Mises stresses is not changed, but this time nonlinear stresses are considered. A new constraint is added to this optimization, enforcing the applied load at the end of the nonlinear analysis, P_{end}, to be equal to the design load, thus avoiding misleading the optimizer if the analysis does not converge to the prescribed load.

In summary, the optimization problem with nonlinear structural stability constraints is defined as

$$
\begin{aligned}
\text{minimize} \quad & m \\
\text{by varying} \quad & t_{\min} \leq [t_{\text{root}}, t_{\text{tip}}] \leq t_{\max} \\
\text{subject to} \quad & g_{\lambda, ij} = -\lambda_{ij} < 0 && i = 1, \ldots, N_i, \ j = 1, \ldots, N_\lambda \\
& g_{\sigma, k} = \sigma_k - \sigma_{\max} < 0 && k = 1, \ldots, N_e \\
& g_P = 0.99 - \frac{P_{\text{end}}}{P_{\text{design}}} < 0
\end{aligned}
\tag{17}
$$

where λ_{ij} is the j-th tangent stiffness matrix eigenvalue at the i-th converged increment, N_i is the number of converged increments and $N_\lambda = 20$. The constraint on the applied load at the end of the nonlinear analysis is implemented as an inequality, where the difference with respect to the prescribed load must be smaller than 1%.

The eigenvalues of the tangent stiffness matrix are also aggregated using a KS function, instead of imposing the constraints on each individual eigenvalue, such that

$$
KS_\lambda = \max_{i,j} \left(g_{\lambda, ij} \right) + \frac{1}{\rho} \ln \left(\sum_{i=1}^{N_i} \sum_{j=1}^{N_\lambda} \exp \left(\rho \left(g_{\lambda, ij} - \max_{i,j} \left(g_{\lambda, ij} \right) \right) \right) \right).
\tag{18}
$$

All computations are performed using MSC Nastran's nonlinear analysis solution sequence, SOL 106. To monitor the 20 smallest magnitude eigenvalues of the tangent stiffness matrix we use a suitable DMAP invoked by the Nastran input file[4].

The arc-length method is set up through the NLPARM and the NLPCI cards, whose settings are reported in Table 2. These settings are chosen with the aim of maximizing the computational efficiency of SOL 106's arc-length solver. The strategy employed consists in starting the nonlinear analysis using a relatively large arc-length increment size and then allowing the increment size to reduce in presence of nonlinearities and to increase again where the equilibrium path is mostly linear. In fact, for small applied loads the equilibrium path can be reliably followed with coarse resolution, while a fine resolution is only needed in presence of nonlinearities. The reader is referred to the MSC Nastran Quick Reference Guide for a detailed explanation on the meaning of the parameters.

Despite being a single-discipline problem, both optimizations are set up in the Open-MDAO framework [29] in view of a future extension to a coupled aeroelastic analysis. Among the optimization algorithms available within the OpenMDAO architecture, the gradient-free COBYLA algorithm is chosen. The pyNastran library[5] is used to interface the Nastran model with the OpenMDAO framework.

---

[4]DMAP stands for Direct Matrix Abstraction Program and is a high-level language with its own compiler and grammatical rules that allows the user to modify MSC Nastran's standard solution sequences to perform custom operations. The computation employs a Lanczos algorithm to find the eigenvalues for each converged increment.

[5]https://github.com/SteveDoyle2/pyNastran, accessed April 2024.

Table 2: Non-default parameters of the NLPARM and NLPCI Nastran cards employed for the nonlinear analyses during the optimization of the CRM-like box beam.

NLPARM field	Value	NLPCI field	Value
KMETHOD	ITER	TYPE	CRIS
KSTEP	-1	MINALR	10^{-5}
MAXITER	3	DESITER	4
CONV	PU	MXINC	300
EPSU	10^{-5}		
EPSP	10^{-6}		
MAXBIS	20		

4 INFLUENCE OF LOAD INTRODUCTION METHOD

4.1 Nonlinear structural stability response of initial structure

To assess the influence of the different load introduction methods, we first analyze their impact on the nonlinear analysis of the initial structure of the CRM-like box beam, which employs a uniform wall thickness throughout. To investigate the nonlinear response of the structure, we apply a load of magnitude twice as big as the design load, $P/P_{\text{design}} = 2$. This preliminary evaluation helps establish a baseline understanding of how the structure behaves under the different load introduction methods without the influence of optimization modifications.

Figure 5 presents a comparative analysis of the linear buckling loads for the initial CRM-like box beam obtained from the different load introduction methods, each normalized against the design load. The linear buckling load obtained when using distributed follower forces is marginally lower, by 0.2%, compared to that using distributed non-follower forces. This minor difference is likely due to slight alterations in load distribution at the skin edges inherent to the transformation of the pressure load over the element into follower forces, as discussed in Section 3.2.

Also the linear buckling load obtained from the non-follower forces applied to the LRA is slightly smaller than that resulting from the distributed non-follower forces, with a percentage difference of 0.4%.
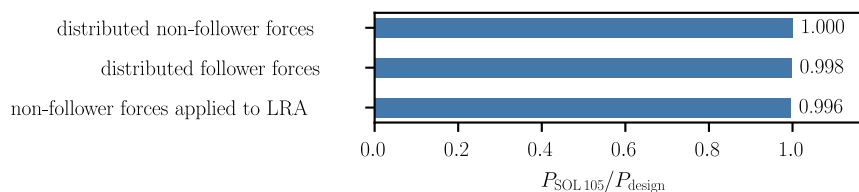
Figure 5: Linear buckling loads of initial structure resulting from the different load introduction methods.

Figure 6 presents a comparison of the root bending moments resulting from the integration of the applied loads along the undeformed CRM-like box beam. The distributed follower forces result in a 0.2% larger root bending moment compared to the distributed non-follower forces. This finding explains the slightly lower linear buckling load discussed earlier, as it suggests that the root region of the top skin is marginally more heavily loaded.

Conversely, the non-follower forces applied to the LRA result in an almost identical root bending moment compared to the distributed non-follower forces. This outcome does not

correlate with the previously observed smaller linear buckling load. Such a discrepancy suggests that the LRA approach provides a conservative assessment of the linear buckling load, as for the same root bending moment the linear analysis predicts the structure to buckle earlier than that subjected to distributed forces.
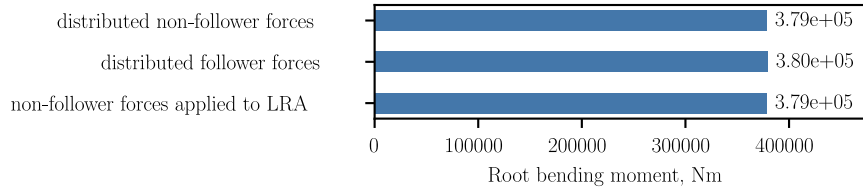

Figure 6: Root bending moments resulting from the different load introduction methods.

Figure 7 depicts the load-displacement response of the CRM-like box beam for the different load introduction methods, focusing on the tip displacement and the displacement at the node of the root region shown in Fig. 3. These displacements are nondimensionalized by the length and the width of the CRM-like box beam, respectively.

The diagram of the root displacement reveals that, for all methods, there is a marked increase in displacement relative to the initial response as the nondimensional applied load P/P_{design} approaches and surpasses 1. Notably, despite the significant displacement increases, the structure does not exhibit any neutral equilibrium points indicative of buckling, thus maintaining stability across all analyzed equilibrium points.

This behavior typifies a broken supercritical pitchfork, where the mechanical asymmetry induced by bending loads leads to a single natural stable equilibrium path instead of the three post-buckling paths typically seen at a bifurcation point. The structural response obtained with distributed non-follower and follower forces closely align. However, the curve corresponding to non-follower forces applied to the LRA displays an almost symmetrical response, revealing the inaccuracy of this approach for nonlinear predictions.

Regarding the tip displacement, the curve of the LRA-applied forces displays a less steep slope, indicating a globally more compliant structural response compared to that obtained with distributed forces.
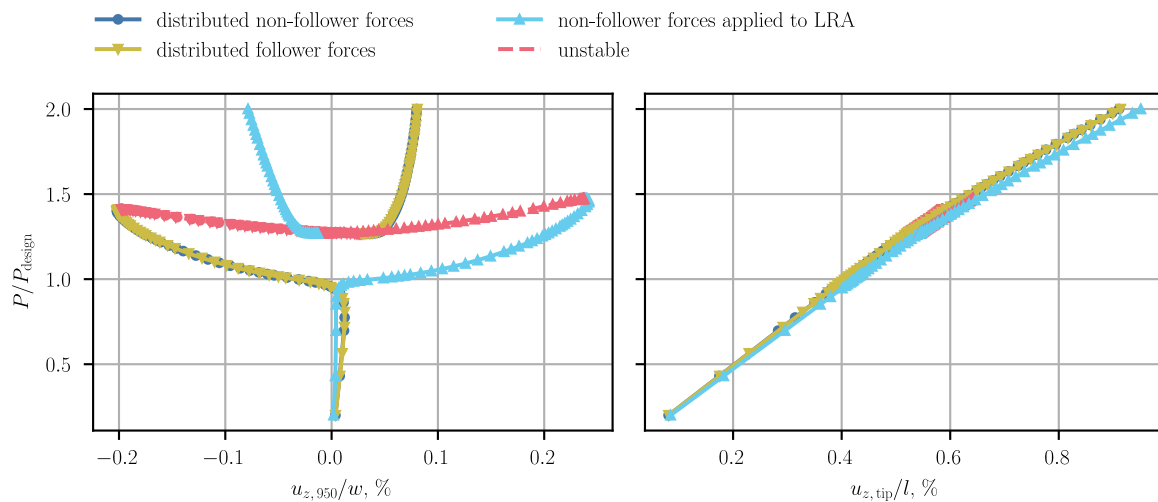
Figure 7: Load-displacement diagrams of initial structure.

All three scenarios exhibit loss of stability at a load limit point, occurring well beyond

the linear buckling load determined for each case. Figure 8 provides a comparison of the limit point loads for the CRM-like box beam. The limit point load obtained from distributed follower forces shows a negligible reduction of 0.1% compared to that obtained from distributed non-follower forces. This small difference aligns with the previous finding of the marginally smaller linear buckling load and larger root bending moment.

Instead, the limit point load obtained using non-follower forces applied to the LRA is significantly higher, at 4.3% above that of the distributed non-follower forces. This result contradicts the previous finding of the linear buckling analysis, where the LRA-load resulted in a lower critical load with respect to the distributed forces. Instead, the non-linear analysis predicts a higher critical load when the LRA load introduction method is employed, thus providing non-conservative results compared to the distributed forces.
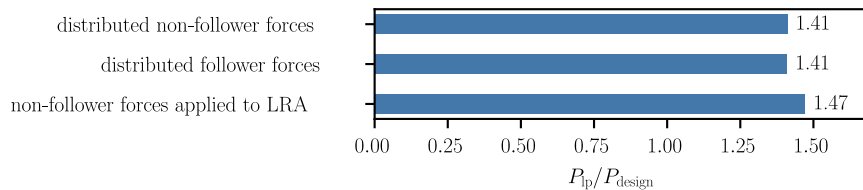
Figure 8: Limit point loads resulting from the different load introduction methods.

Figure 9 illustrates the deformation of the CRM-like box beam under distributed non-follower forces and non-follower forces applied to the LRA at the respective limit point load. This comparison highlights a distinct phase shift in the buckling-like deformation of the top skin between the two load introduction methods.

With the distributed non-follower forces, the deformation manifests a negative rotation about the x-axis at the center of the root of the first rib-stiffener bay. Conversely, for the non-follower forces applied to the LRA, there is a positive rotation at the same location. This phase shift reflects the significant differences observed for the root displacement response in Fig. 7.

(a) Distributed non-follower forces.

(b) Non-follower forces applied to LRA.
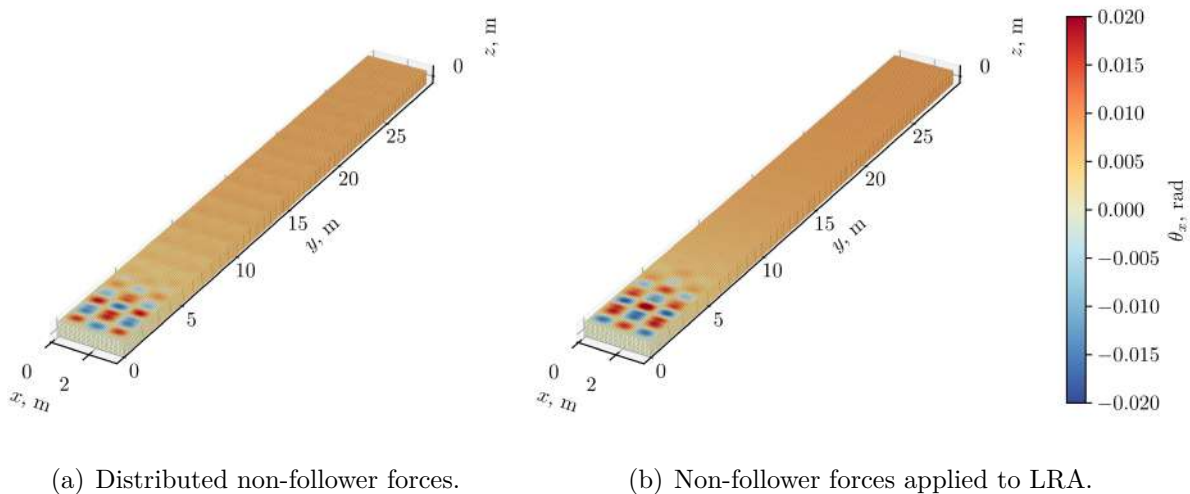
Figure 9: Deformation at limit point load. Elements are colored by their average rotation about the x-axis.

In summary, these findings highlight that despite the LRA approach can result in a

conservative estimation of the critical load when using linear analyses, this might not be true when using nonlinear analyses. In addition, the use of the LRA approach can result in inaccurate nonlinear structural deformations.

Finally, the equilibrium paths obtained with the different load introduction methods indicate that the structure would experience snap-through when loaded past the load limit point. Figure 10 shows the deformations before and after the snap-through event for the case of the distributed non-follower forces. It is possible to observe a change of the deformation within the first rib bay: before the snap the deformation of each rib-stiffener bay is characterized by a single half-wave, while after the snap the deformation is characterized by two half-waves.
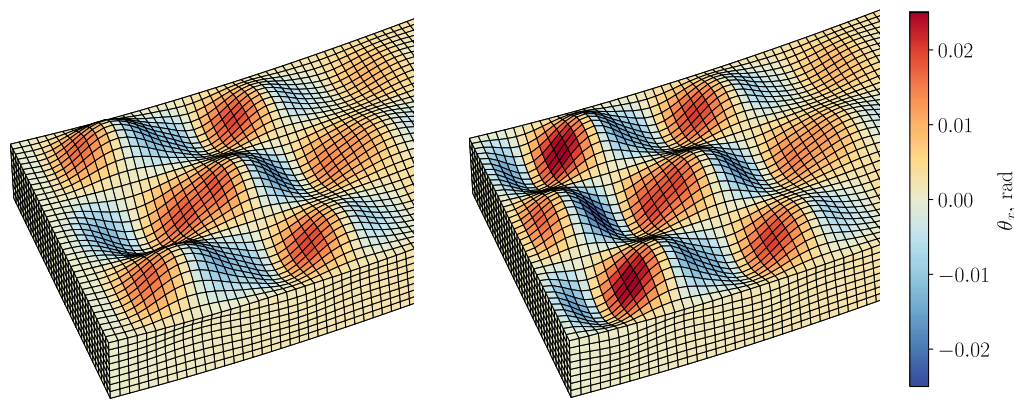
(a) Before snap-through.   (b) After snap-through.

Figure 10: Deformation over the CRM-like box beam root across the snap-through behavior resulting from the analysis with distributed non-follower forces. Displacements are amplified by a factor 50 for visualization purposes. Elements are colored by their average rotation about the x-axis.

4.2 Optimization with distributed non-follower forces

The linear buckling optimization of the model employing distributed non-follower forces results in a 42.2% reduction in mass relative to the initial structure. Under the linear buckling constraint, the optimization pushes the tip thickness to its lower bound, while the root thickness increases compared to the initial design. The subsequent optimization with the nonlinear structural stability constraint leads to a further reduction of 9.3% in mass. Here, while the tip thickness remains at the lower bound, the root thickness is reduced to 7.1 mm, as illustrated in Fig. 11.
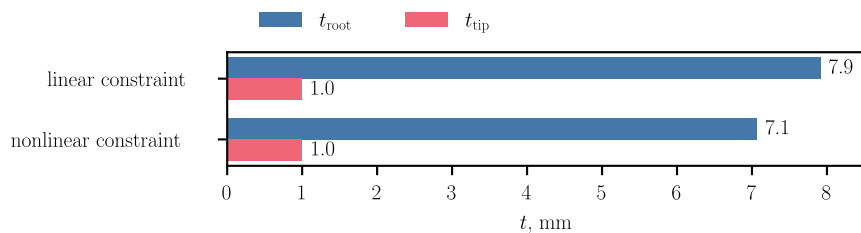
Figure 11: Thicknesses resulting from the optimizations with distributed non-follower forces.

Figure 12 shows the load-displacement diagrams of the initial structure compared to the linearly and the nonlinearly optimized structures. The root displacement responses of

the initial and the linearly optimized structures overlap almost entirely, indicating, as expected, that linear optimization does not introduce a different local behavior. On the other hand, the nonlinearly optimized structure shows a load-displacement curve where local nonlinearities are more developed. This response is analogous to the one shown in Fig. 7, only shifted towards a lower applied load. This suggests that the nonlinear optimization effectively exploits the full structure's nonlinear stability capacity, aligning the load limit point with the design load.

The tip displacement diagram shows a reduced slope of the load-displacement curve through the linear buckling optimization and a further diminished slope under the nonlinear structural stability constraint. Notably, the glass ceiling of linear buckling for the nonlinearly optimized structure is found at $P/P_{\text{design}} = 0.72$, with a visible nonlinearity in the tip displacement response as the applied load exceeds this point. This change is attributed to buckling-like deformation patterns emerging across the root region of the top skin.
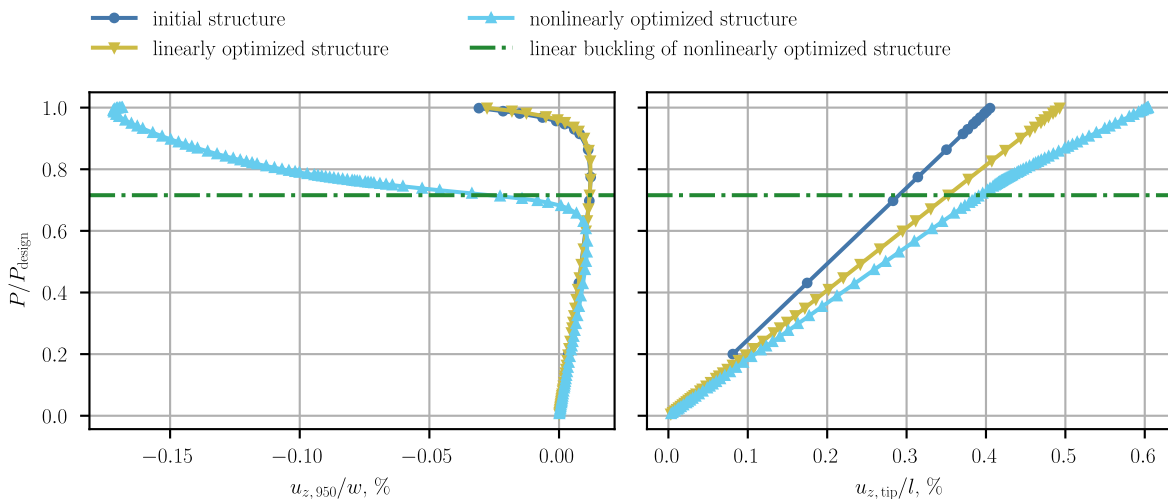
Figure 12: Load-displacement diagrams resulting from the optimizations with distributed non-follower forces.

Figure 13 compares the deformation at the design load of the linearly and nonlinearly optimized structures. It can be observed that the nonlinearly optimized structure exhibits a pronounced buckling-like deformation over the top skin, absent in the linearly optimized version. This deformation signifies a more efficient material use that taps into the nonlinear stability capacity of the structure, thereby allowing the further mass reduction from the linearly optimized structure. As far as the rotations observed towards the tip region of the top skin in both cases, these are not associated to a buckling-like deformation, rather they are a direct consequence of the distributed non-follower forces pulling up the parts of the skin not supported by ribs.

4.3 Optimization with distributed follower forces

The optimization studies carried out on the model employing distributed follower forces achieve results very similar to those observed with distributed non-follower forces, as can be observed from the optimized thickness distributions shown in Fig. 14. In this case the optimization under linear buckling constraints results in a mass reduction of 42.1% compared to the initial design. Subsequent optimization with nonlinear structural stability constraints enables an additional mass reduction of 9.3%.

The load-displacement behavior and the deformation at the design load are totally analogous to those achieved with non-follower forces, as it can be observed in Fig. 15 and 16, respectively.

4.4 Optimization with non-follower forces applied to load reference axis

The linear buckling optimization of the model employing non-follower forces applied to the LRA leads to a mass reduction of 39.3% compared to the initial design. This mass
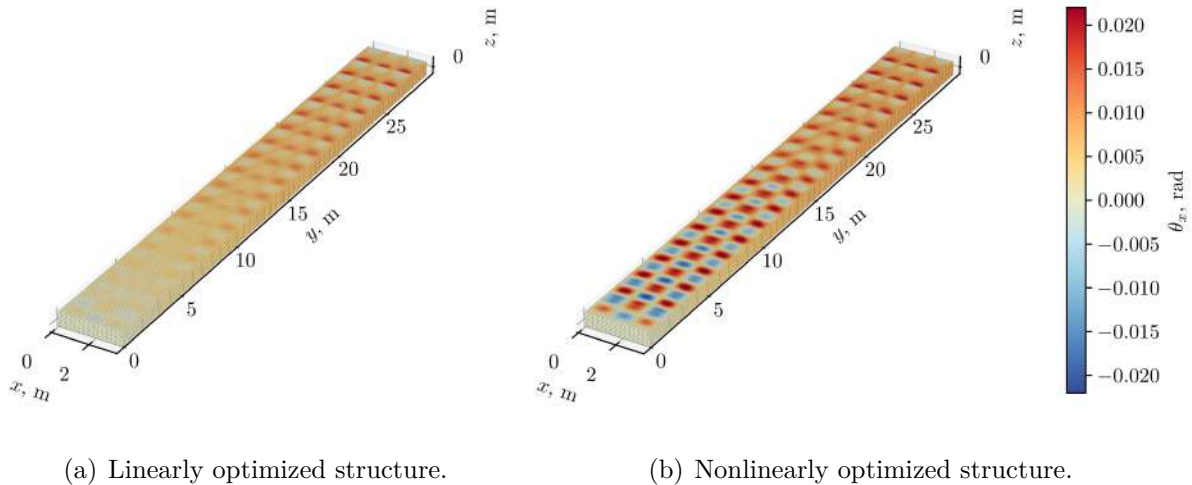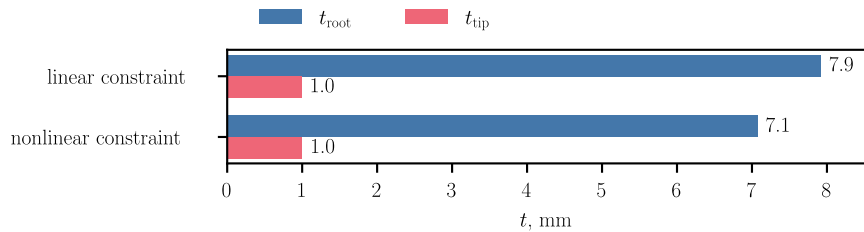

(a) Linearly optimized structure.
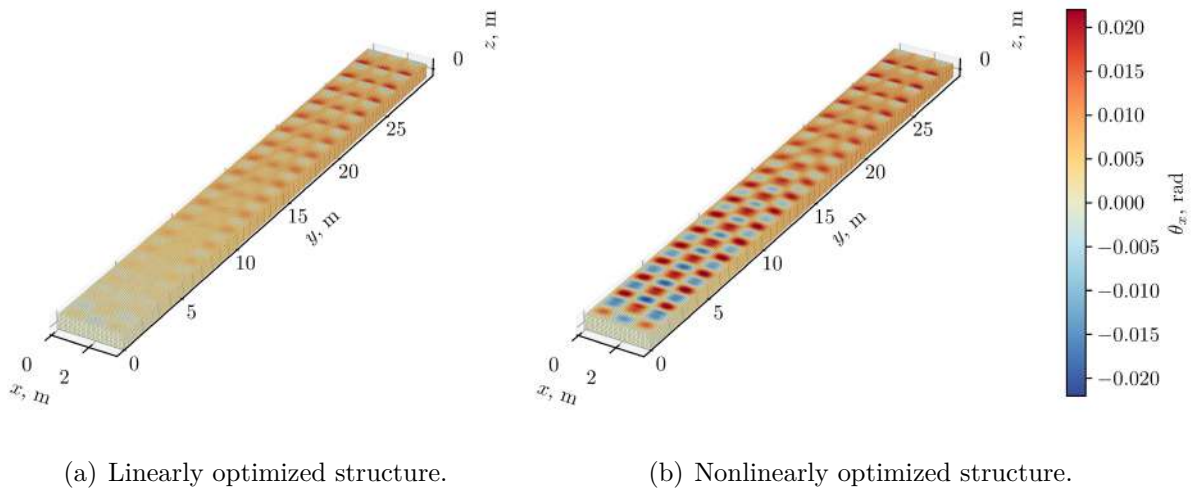
(b) Nonlinearly optimized structure.

Figure 13: Deformations at design load resulting from the optimizations with distributed non-follower forces. Elements are colored by their average rotation about the x-axis.

Figure 14: Thicknesses resulting from the optimizations with distributed follower forces.
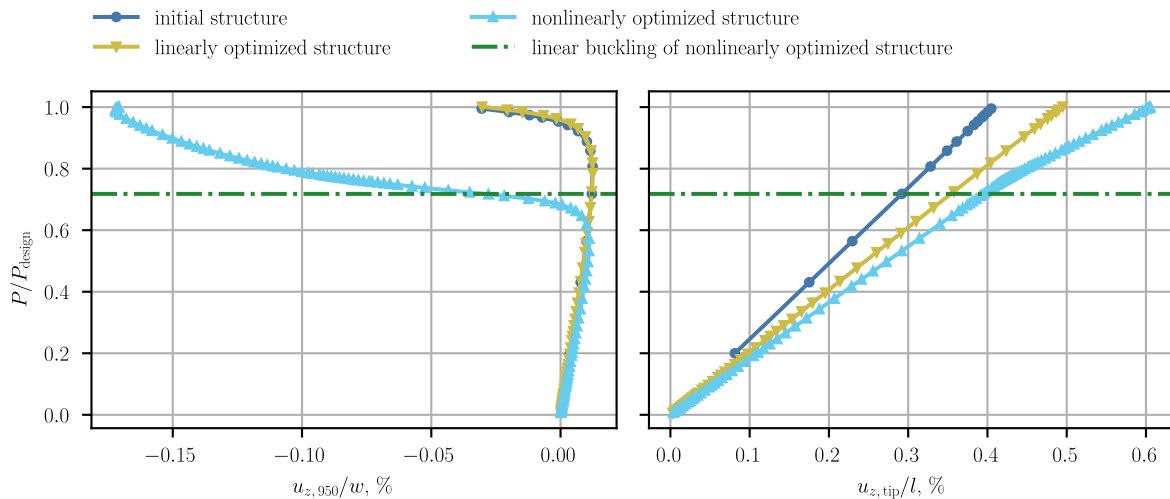
Figure 15: Load-displacement diagrams resulting from the optimizations with distributed follower forces.

18

reduction is smaller with respect to that obtained in the previous cases, and it aligns with the conservative linear buckling prediction found in Sec. 4.1. Successively, the optimization with the nonlinear structural stability constraint achieves an additional mass reduction of 8.3%. Figure 17 illustrates the resulting thickness distribution, where the root thickness maintain the same trend observed in the previous optimization studies, that is to say an increase under the linear buckling constraint and a decrease under the nonlinear structural stability constraint. However, in this case the tip thickness does not reach the lower bound after the first optimization, and it only does so after the second optimization.

The load-displacement diagrams, as shown in Fig. 18, reflect a similar structural response as seen in the previous cases but with a notable difference: the root displacements are mirrored to positive values. This variation is consistent with the loading characteristics introduced by the LRA method in the initial structure, as indicated in Fig. 7. In this case, the glass ceiling of linear buckling for the nonlinearly optimized structure is placed at $P_{\text{SOL 105}}/P_{\text{design}} = 0.44$.

The deformations at the design load, depicted in Fig. 19, show results similar to the previous optimization cases. The nonlinearly optimized structure again exhibits a buckling-like deformation pattern on the top skin, although with a smaller rotation of the elements closer to the root. This deformation pattern is absent in the linearly optimized structure. Notably, the deformations induced by pulling on the unsupported parts of the skin are

(a) Linearly optimized structure. (b) Nonlinearly optimized structure.

Figure 16: Deformations at design load resulting from the optimizations with distributed follower forces. Elements are colored by their average rotation about the x-axis.
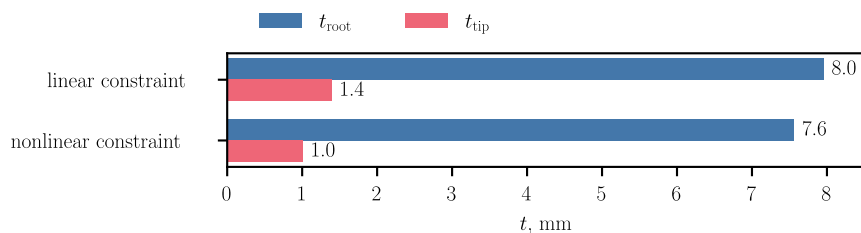

Figure 17: Thicknesses resulting from the optimizations with non-follower forces applied to LRA.

not present in this case due to the application of the loads via the LRA.

Finally, when comparing the buckling-like deformation patterns of the nonlinearly optimized structure from this scenario with those from previous cases, the same phase shift observed in Fig. 9 for the initial design is evident.

4.5 Comparative discussion

Figure 20 shows the final mass resulting from each optimization. The results reveal very close mass reductions for optimizations using distributed non-follower and follower forces. Specifically, the optimization with distributed non-follower forces leads to an overall 47.6% reduction in mass from the initial design, while the optimization with distributed follower forces achieves a slightly smaller reduction of 47.5%. This outcome might be justified by the root bending moment resulting from the follower forces being slightly larger, as indicated in Fig. 6.
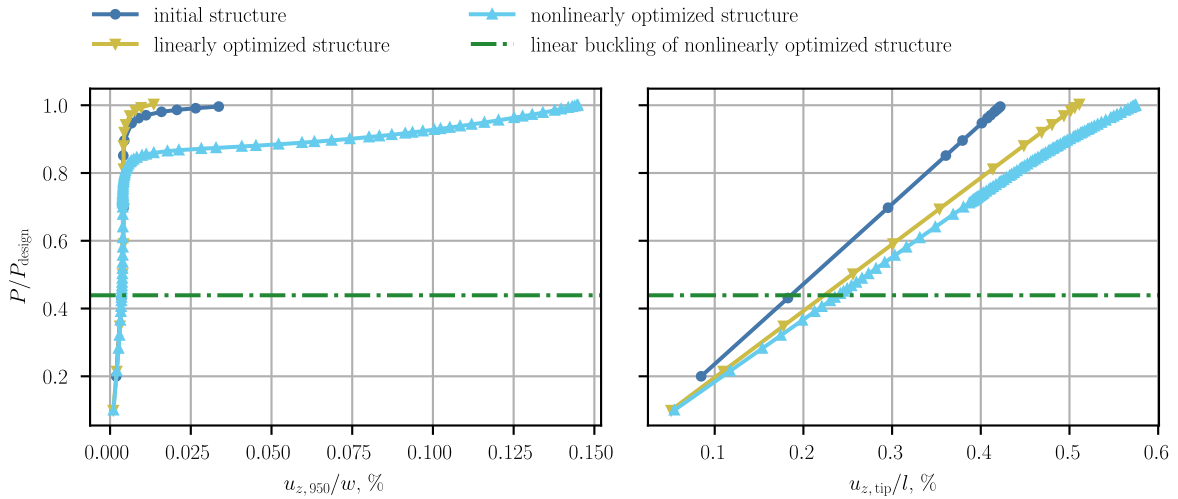
Figure 18: Load-displacement diagrams resulting from the optimizations with non-follower forces applied to LRA.
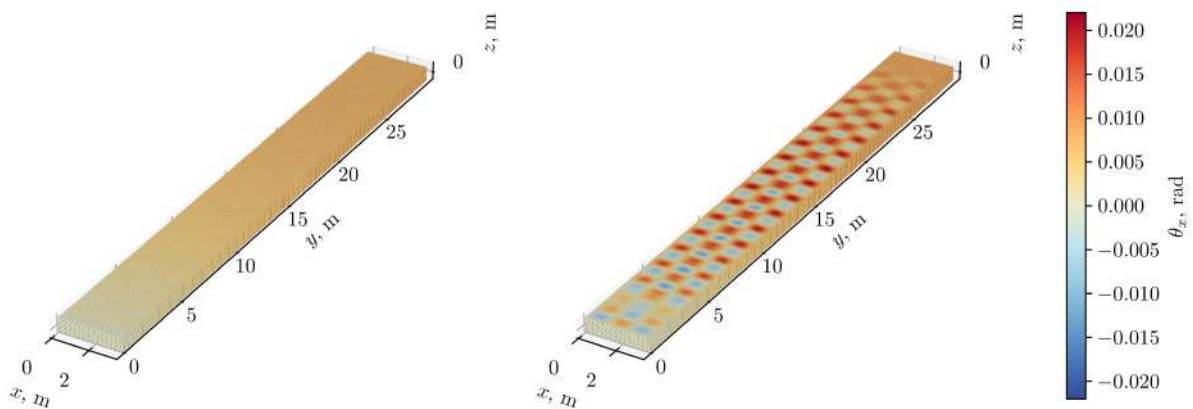
(a) Linearly optimized structure.

(b) Nonlinearly optimized structure.

Figure 19: Deformations at design load resulting from the optimizations with non-follower forces applied to LRA. Elements are colored by their average rotation about the x-axis.

Nonetheless, the difference between the distributed non-follower and follower forces optimizations is too small to draw any definitive conclusion. These results should be further validated through analogous optimization studies on cases where the structure exhibits a larger deflection, as the effects of follower forces are expected to be more pronounced.

The optimizations with non-follower forces applied to the LRA result in smaller mass reductions compared to the other two load introduction methods. This outcome is expected for the optimization with linear buckling constraints, given the conservative prediction of the linear buckling load when employing the LRA approach, but it is unexpected for the optimization with nonlinear structural stability constraints, as in the initial structure the limit point load obtained with the LRA approach was higher compared to those obtained with the other approaches. Evidently, this comparison changes as the thickness assumes a linear variation from root to tip. Despite the fact that the final mass obtained employing the LRA approach is larger with respect to the other methods, and thus conservative, these findings suggest that when assessing the nonlinear structural stability of a wingbox structure, the LRA approach should be avoided to obtain reliable deformation results.
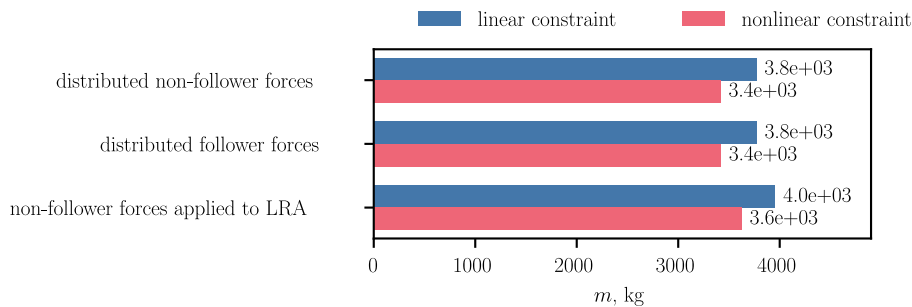
Figure 20: Masses resulting from the different optimizations.

5 CONCLUSION

This paper reinforced the advantages of integrating nonlinear structural stability constraints within optimization frameworks for wingbox structures, demonstrating the approach with a distributed load and a linearly varying thickness from root to tip. Three distinct load introduction methods were considered to study their influence on the nonlinear response and on the optimization results: distributed non-follower forces, distributed follower forces, and non-follower forces applied to a load reference axis.

The nonlinear structural stability constraint, already used in previous works, was revised to accommodate the presence of follower forces. This revision involved the assessment of the positive definiteness of the quadratic form of the tangent stiffness matrix by examining the eigenvalues of the symmetrized matrix.

The analyses and optimization studies were performed on an idealized version of the Common Research Model wingbox, also used in previous works. The nonlinear analyses of the initial structure revealed that the use of non-follower forces applied to the load reference axis resulted in non-conservative estimates of structural stability, which suggested that such methods may overpredict the nonlinear structural stability capacity, leading to potentially unsafe designs.

The optimization results highlighted the benefits of the nonlinear structural stability approach, showing mass reduction ranging between 8 and 9% with respect to the linearly

optimized structure in all considered cases. Only a small difference was observed between the optimizations with distributed non-follower and follower forces, with the latter providing a marginally smaller overall mass reduction with respect to the initial design. This finding should be validated by studying cases displaying a larger deflection of the wingbox, where the effect of the follower forces is expected to be more prominent.

Contrary to what is observed for the initial structure, the optimization with non-follower forces applied to the load reference axis resulted in smaller mass reduction compared to the other methods, suggesting that when a linear thickness variation is considered the load reference axis approach provides conservative results.

Future research will continue to expand on these findings, exploring more realistic optimization scenarios, including the presence of curved skin, more complex loading conditions, and by integrating an aerodynamic solver to simulate a truly aeroelastic case. This ongoing work aims to advance the structural stability approach of aeroelastic optimization frameworks and push the boundaries of what is achievable in the design of next-generation aerospace structures.

APPENDIX

A mesh convergence study is performed by running the MSC Nastran linear buckling solution sequence, SOL 105, on the model with distributed non-follower forces applying a load $P = 1\,\mathrm{N}$. Increasing mesh resolutions are considered and the predicted linear buckling load, $P_{\mathrm{SOL\ 105}}$, is monitored. The results of the mesh convergence study are shown in Fig. 21. The mesh is defined to be converged when the difference of the linear buckling load with respect to the one obtained with the finest mesh is below 1%.
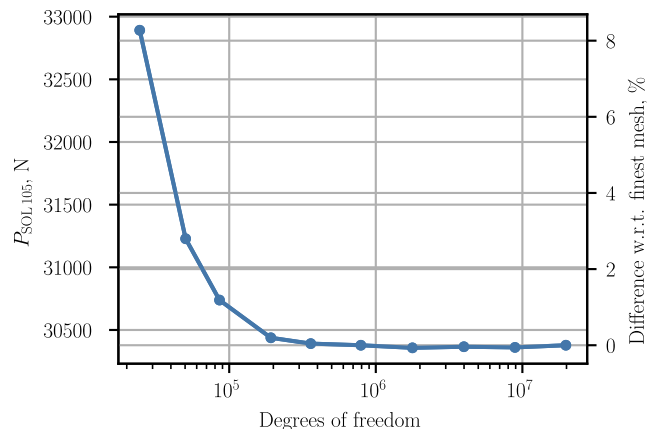

Figure 21: Mesh convergence study of the CRM-like box beam model under distributed non-follower forces.

Since the mesh convergence study is executed with the use of linear buckling analyses, the convergence of the mesh is verified in the nonlinear regime. To do this, two nonlinear analyses are performed, one using the original mesh resulting from the convergence study and another one using a refined mesh generated by choosing a target element length equal to half the element length used for the original mesh. The applied load is set to twice the linear buckling load obtained for the original mesh to capture the nonlinear region of the structural response.

The results of these analyses are shown in Fig. 22 in terms of a 3D load-displacement diagram combining the local displacement at the root, the tip displacement, and the

applied load. The local displacement at the root is evaluated for both models at the node where each linear buckling analysis predicts the maximum displacement for the critical buckling mode. For the model employing the original mesh, this node is shown in Fig. 3, and its position is analogous for the model employing the refined mesh.

It can be observed that the two analyses predict the same behavior up to the unstable part of the equilibrium path, where the results start diverging. In particular, the model with the refined mesh appears to show a higher-order unstable response. Nonetheless, there is a good agreement between the limit point loads, with that of the model employing the original mesh being only 0.7% higher than the limit point load of the model employing the refined mesh. This result suggests that the original mesh is detailed enough to capture the part of the nonlinear response of the CRM-like box beam that is of interest for the optimization studies.
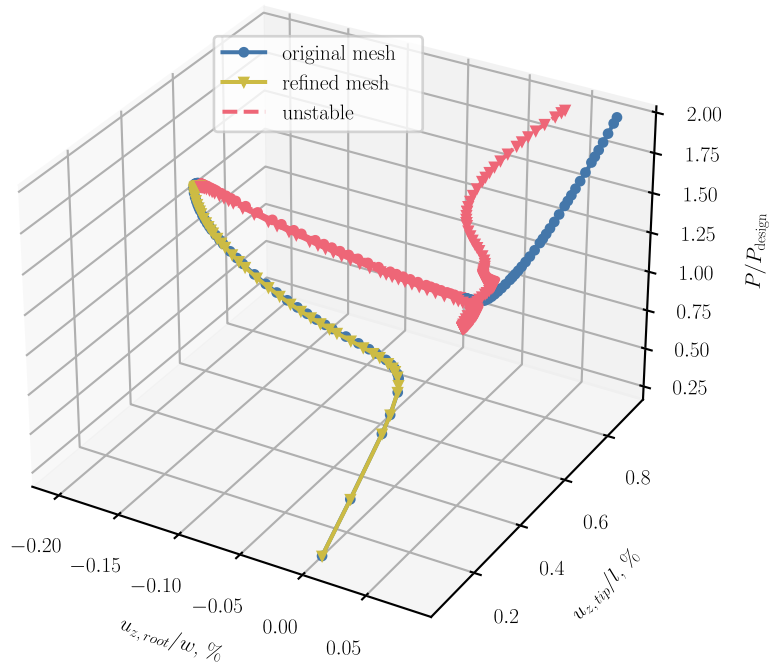
Figure 22: Load-displacement diagrams obtained with the original and the refined mesh of the CRM-like box beam.

The histories of the optimizations performed for this paper are shown in Figs. from 23 to 28. Since the COBYLA algorithm does not always end the optimization on a design point satisfying all the constraints, the results shown in this paper are always related to the last feasible design point.
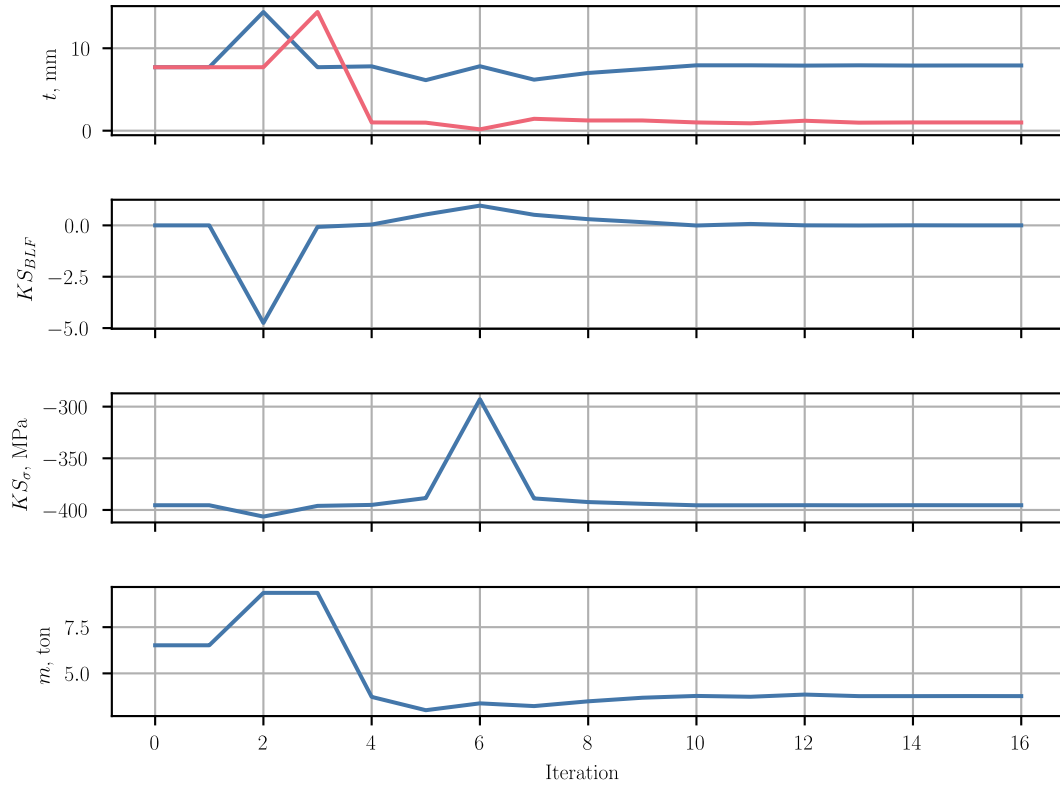
Figure 23: Linear buckling optimization history for the model employing distributed non-follower forces.
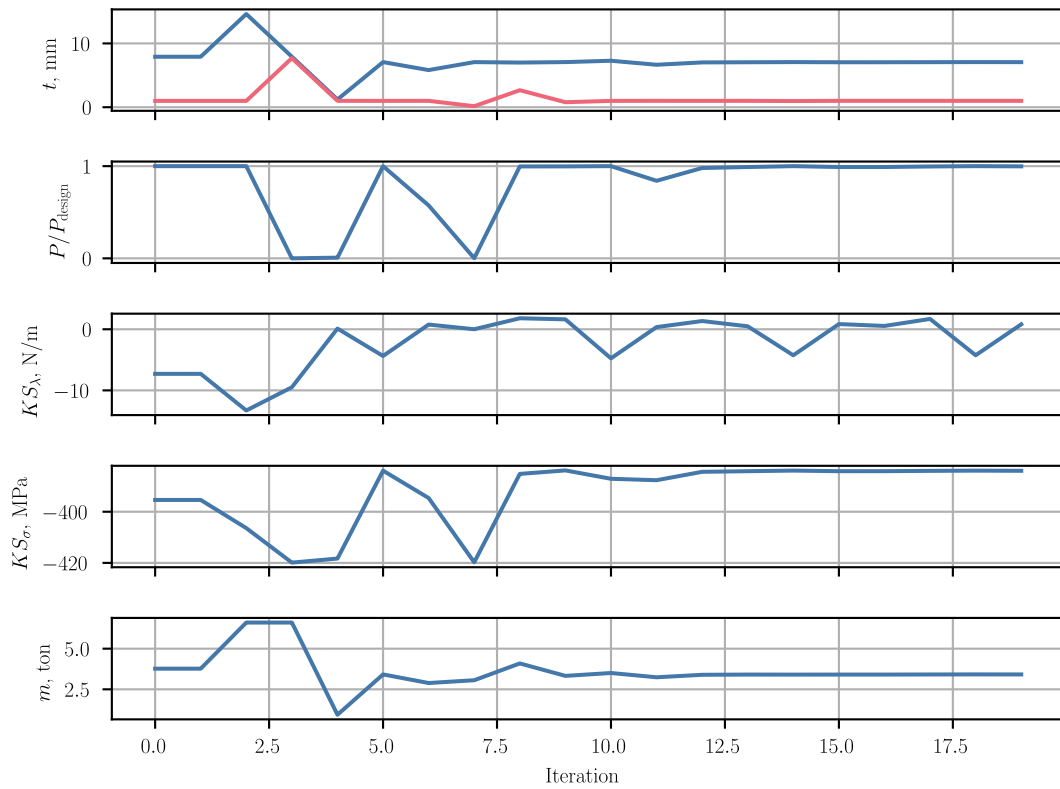

Figure 24: Nonlinear structural stability optimization history for the model employing distributed non-follower forces.
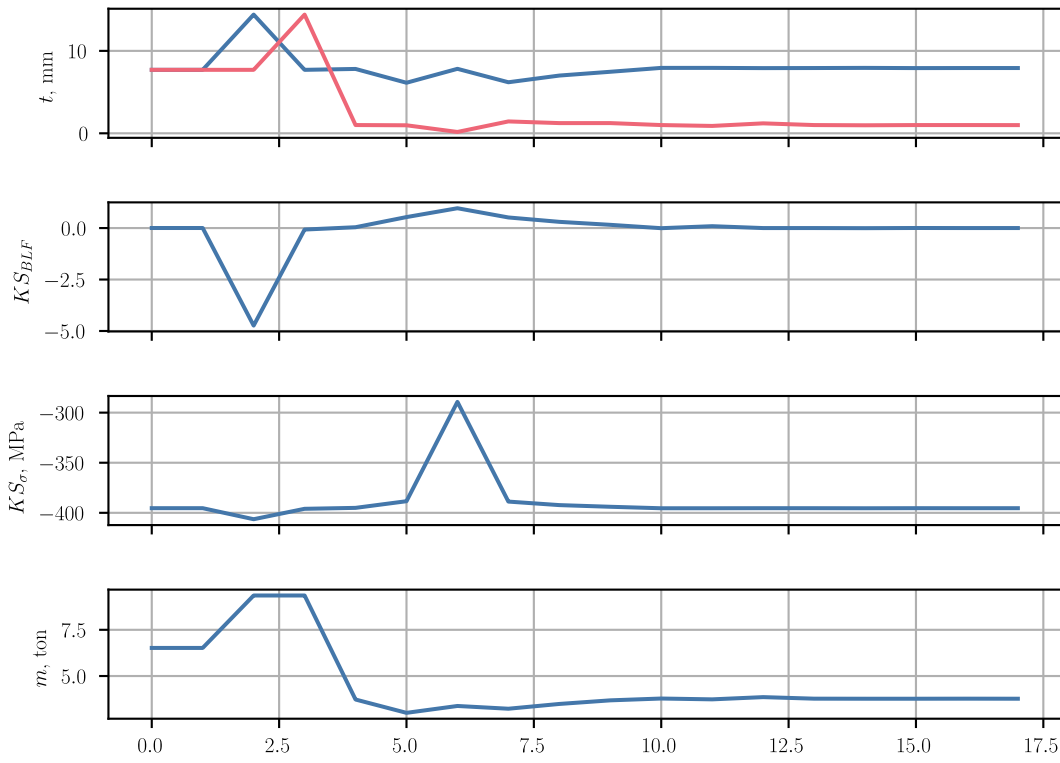
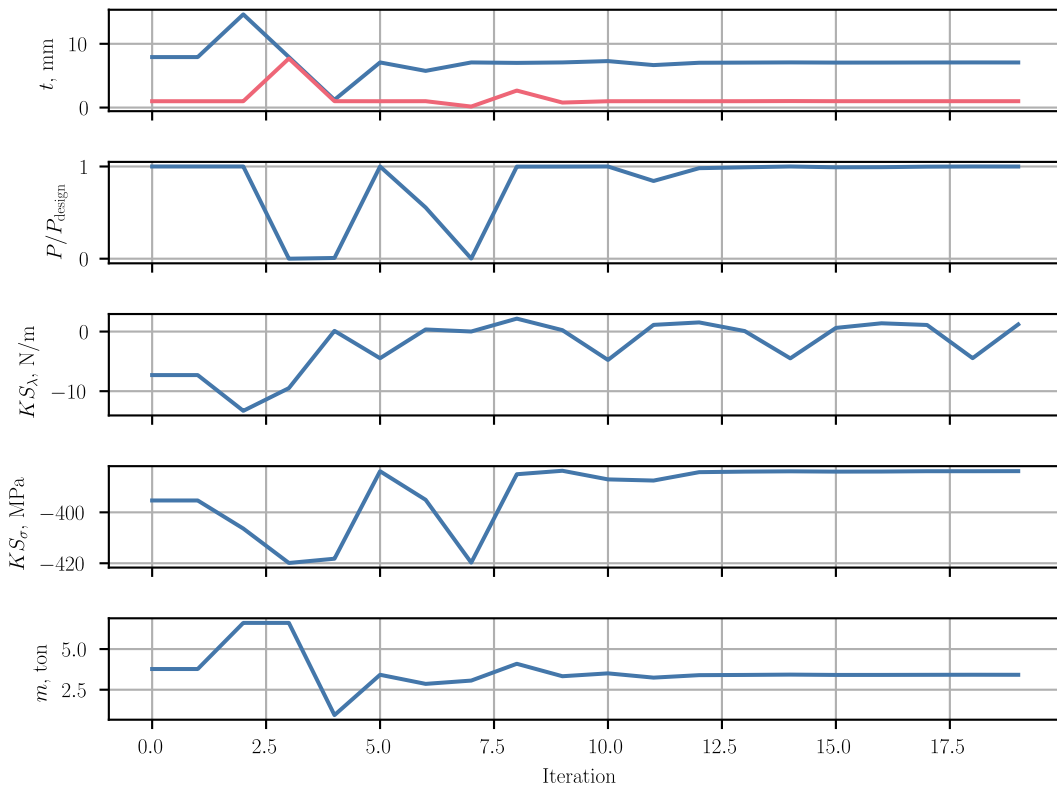Figure 25: Linear buckling optimization history for the model employing distributed follower forces.

Figure 26: Nonlinear structural stability optimization history for the model employing distributed follower forces.
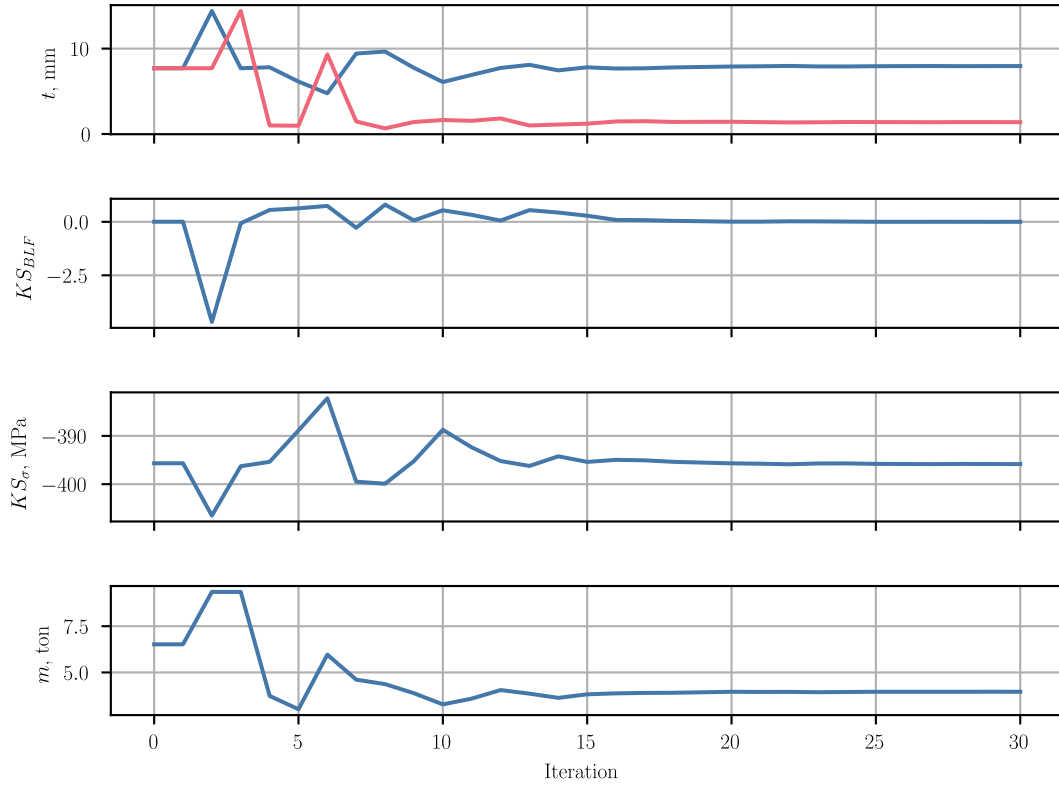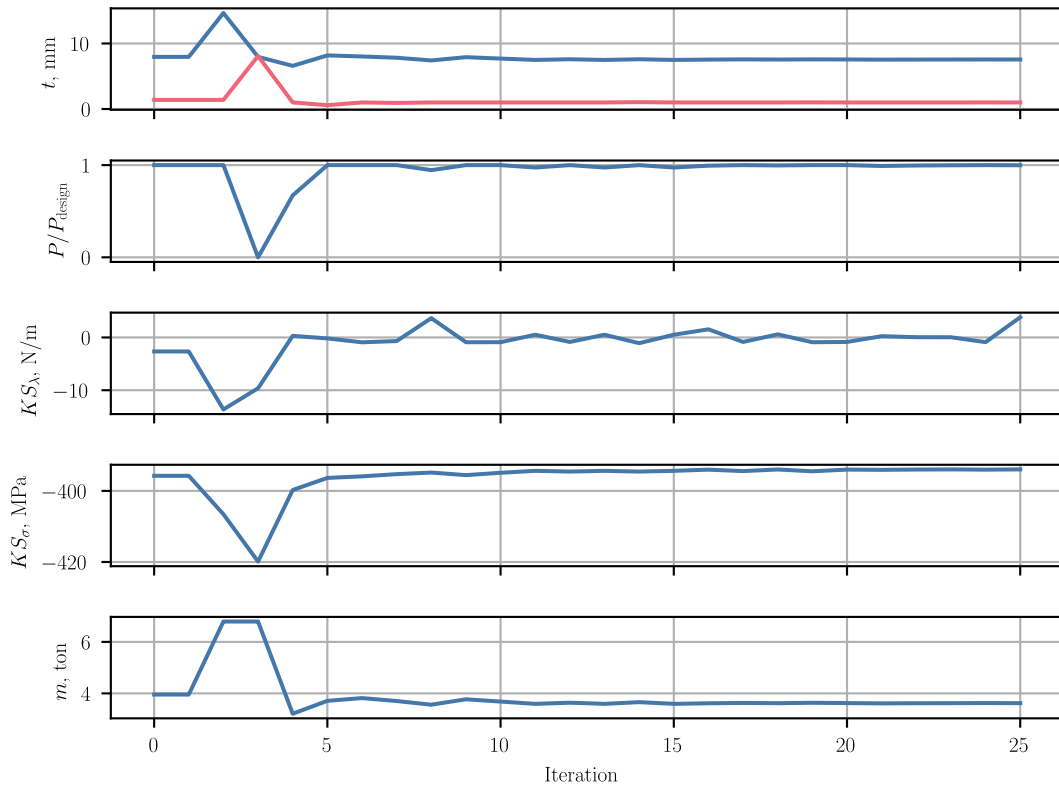
Figure 27: Linear buckling optimization history for the model employing non-follower forces applied to the LRA.

Figure 28: Nonlinear structural stability optimization history for the model employing non-follower forces applied to the LRA.

6 REFERENCES

[1] (2021). Commitment to Fly Net Zero. https://aviationbenefits.org/flynetzero/. Accessed November 2023.

[2] Filippone, A. (2006). Flight Performance of Fixed and Rotary Wing Aircraft. Elsevier. ISBN 09780750668170.

[3] Dillinger, J. K. S., Klimmek, T., Abdalla, M. M., et al. (2013). Stiffness optimization of composite wings with aeroelastic constraints. Journal of Aircraft, 50(4), 1159–1168. doi:10.2514/1.C032084.

[4] Stanford, B. K., Jutte, C. V., and Wieseman, C. D. (2016). Trim and structural optimization of subsonic transport wings using nonconventional aeroelastic tailoring. AIAA Journal, 54(1), 293–309. doi:10.2514/1.J054244.

[5] Stodieck, O., Cooper, J. E., Weaver, P. M., et al. (2017). Aeroelastic tailoring of a representative wing box using tow-steered composites. AIAA Journal, 55(4), 1425–1439. doi:10.2514/1.J055364.

[6] Stanford, B. K. and Jutte, C. V. (2017). Comparison of curvilinear stiffeners and tow steered composites for aeroelastic tailoring of aircraft wings. Computers & Structures, 183, 48–60. ISSN 0045-7949. doi:https://doi.org/10.1016/j.compstruc.2017.01.010.

[7] Othman, M. F., Silva, G. H., Cabral, P. H., et al. (2019). A robust and reliability-based aeroelastic tailoring framework for composite aircraft wings. Composite Structures, 208, 101–113. ISSN 0263-8223. doi:https://doi.org/10.1016/j.compstruct.2018.09.086.

[8] De, S., Jrad, M., and Kapania, R. K. (2019). Structural optimization of internal structure of aircraft wings with curvilinear spars and ribs. Journal of Aircraft, 56(2), 707–718. doi:10.2514/1.C034818.

[9] Brooks, T. R., Martins, J. R., and Kennedy, G. J. (2019). High-fidelity aerostructural optimization of tow-steered composite wings. Journal of Fluids and Structures, 88, 122–147. ISSN 0889-9746. doi:https://doi.org/10.1016/j.jfluidstructs.2019.04.005.

[10] Krupa, E. P., Cooper, J. E., Pirrera, A., et al. (2018). Improved aerostructural performance via aeroservoelastic tailoring of a composite wing. The Aeronautical Journal, 122(1255), 1442–1474. doi:10.1017/aer.2018.66.

[11] Silva, G. H. C., do Prado, A. P., Cabral, P. H., et al. (2019). Tailoring of a composite regional jet wing using the slice and swap method. Journal of Aircraft, 56(3), 990–1004. doi:10.2514/1.C035094.

[12] Rajpal, D., Gillebaart, E., and De Breuker, R. (2019). Preliminary aeroelastic design of composite wings subjected to critical gust loads. Aerospace Science and Technology, 85, 96–112. ISSN 1270-9638. doi:https://doi.org/10.1016/j.ast.2018.11.051.

[13] Bordogna, M. T., Lancelot, P., Bettebghor, D., et al. (2020). Static and dynamic aeroelastic tailoring with composite blending and manoeuvre load alleviation. Structural and Multidisciplinary Optimization, 61(5), 2193–2216. ISSN 1615-1488. doi: 10.1007/s00158-019-02446-w.

[14] Brooks, T. R. and Smith, B. D. (2020). Aerostructural design optimization of the D8 aircraft using active aeroelastic tailoring. doi:10.2514/6.2020-1967.

[15] Gray, A. C. and Martins, J. R. (2021). Geometrically Nonlinear High-fidelity Aerostructural Optimization for Highly Flexible Wings. doi:10.2514/6.2021-0283.

[16] Niu, M. (1988). Airframe Structural Design. Hong Kong: Conmilit Press, Ltd. ISBN 9789627128045.

[17] Mitrotta, F. M. A., Pirrera, A., Terence, M., et al. (2023, submitted). Proof of concept of a nonlinear structural stability constraint for aeroelastic optimization. The Aeronautical Journal.

[18] Vassberg, J., Dehaan, M., Rivers, M., et al. (2008). Development of a Common Research Model for Applied CFD Validation Studies. doi:10.2514/6.2008-6919.

[19] Mitrotta, F. M. A., Pirrera, A., Macquart, T., et al. Development of a Nonlinear Structural Stability Constraint for Aeroelastic Optimization. doi:10.2514/6. 2024-2412.

[20] Werter, N. and De Breuker, R. (2016). A novel dynamic aeroelastic framework for aeroelastic tailoring and structural optimisation. Composite Structures, 158, 369–386. ISSN 0263-8223. doi:https://doi.org/10.1016/j.compstruct.2016.09.044.

[21] Bažant, Z. P. and Cedolin, L. (2010). Stability of Structures. WORLD SCIENTIFIC. doi:10.1142/7828.

[22] Lerbet, J., Absi, E., and Rigolot, A. (2009). About the stability of nonconservative undamped elastic systems: Some new elements. International Journal of Structural Stability and Dynamics, 09(02), 357–367. doi:10.1142/S0219455409003065.

[23] Leon, S. E., Paulino, G. H., Pereira, A., et al. (2012). A Unified Library of Nonlinear Solution Schemes. Applied Mechanics Reviews, 64(4). ISSN 0003-6900. doi:10.1115/ 1.4006992. 040803.

[24] Schwlizerhof, K. and Ramm, E. (1984). Displacement dependent pressure loads in nonlinear finite element analyses. Computers & Structures, 18(6), 1099–1114. ISSN 0045-7949. doi:https://doi.org/10.1016/0045-7949(84)90154-8.

[25] Taylor, J. D. and Hunsaker, D. F. (2021). Characterization of the Common Research Model Wing for Low-Fidelity Aerostructural Analysis. doi:10.2514/6.2021-1591.

[26] Brooks, T. R., Kenway, G. K. W., and Martins, J. R. R. A. (2018). Benchmark aerostructural models for the study of transonic aircraft wings. AIAA Journal, 56(7), 2840–2855. doi:10.2514/1.J056603.

[27] Kiviaho, J. F. and Kennedy, G. J. (2019). Efficient and robust load and displacement transfer scheme using weighted least squares. AIAA Journal, 57(5), 2237–2243. doi: 10.2514/1.J057318.

[28] Martins, J. R. R. A. and Ning, A. (2022). Engineering Design Optimization. Cambridge University Press. ISBN 9781108833417.

[29] Gray, J. S., Hwang, J. T., Martins, J. R. R. A., et al. (2019). OpenMDAO: An Open-Source Framework for Multidisciplinary Design, Analysis, and Optimization. Structural and Multidisciplinary Optimization, 59, 1075–1104. doi: 10.1007/s00158-019-02211-z.

COPYRIGHT STATEMENT